Terahertz field driven nonlinear Hall effect and other second order transport phenomena in two-dimensional tellurene

M. D. Moldavskaya,[1] L. E. Golub,[2] E. Mönch,[1] Chang Niu,[3,4] Peide D. Ye,[3,4] J. Wunderlich,[1] and S. D. Ganichev[1,5,*]

[1]*Physics Department, University of Regensburg, 93040 Regensburg, Germany*
[2]*Institute of Theoretical Physics and Halle-Berlin-Regensburg Cluster of Excellence CCE, University of Regensburg, 93040 Regensburg, Germany*
[3]*Elmore Family School of Electrical and Computer Engineering, Purdue University, West Lafayette, Indiana 47907, USA*
[4]*Birck Nanotechnology Center, Purdue University, West Lafayette, Indiana 47907, USA*
[5]*CENTERA Labs, Institute of High Pressure Physics, PAS, 01-142 Warsaw, Poland*

(Received 13 July 2026; revised 14 September 2026; accepted 29 October 2026; published 12 November 2026)

We study terahertz field-driven second order nonlinear electron transport phenomena, including the nonlinear Hall effect (NLHE), in two-dimensional tellurene flakes. The dc current excited by linearly polarized terahertz (THz) radiation in Hall bar samples is investigated in directions both along and perpendicular to the c axis of tellurene. As expected for second order transport phenomena, the current scales as the square of the in-plane electric field of the radiation $\boldsymbol{E}$, and depends on its orientation. The current results from a combination of three contributions, including the NLHE, the Nonlinear Longitudinal (NLL) and Nonlinear Diagonal (NLD) currents. We established the equivalence between NLH, NLL, and NLD transport currents and Linear photogalvanic effect (LPGE) contributions induced by the absorption of linearly polarized and unpolarized THz radiation. All contributions can be controlled by a gate voltage and have opposite signs for electron and hole conductivity. The magnitude of the current increases drastically when the samples are cooled from room temperature to 4.2 K. It also increases with decreasing radiation frequency. These results are well described by the developed phenomenological and microscopic theories. We show that the THz radiation-induced electric current originates from microscopic mechanisms such as skew scattering, side jump, and the Berry curvature dipole.

DOI: 10.1103/w8fp-vmm7

I. INTRODUCTION

Tellurene, the two-dimensional (2D) allotrope of trigonal tellurium, has recently emerged as an experimentally accessible elemental semiconductor, enriching the family of low-dimensional van der Waals materials with a structurally and functionally distinct system [1–5]. Since trigonal Te is chiral and lacks inversion symmetry, tellurene hosts chirality-dependent electronic and optical responses and provides a natural platform for studying symmetry-allowed nonlinear transport. In n-type material, Weyl points are located near the band edge and, together with the associated Berry-curvature hot spots, make tellurene particularly attractive in the context of topological quantum materials [6,7]. Beyond its topological aspects, tellurene combines high environmental stability and pronounced catalytic activity [8], gate-tunable carrier density and carrier type [1], a strain-dependent band structure [9], significant piezoelectricity [10,11], a strongly anisotropic photoresponse [12], low thermal conductivity, and room-temperature carrier mobilities close to 10^3 cm^2/Vs [13]. A variety of intriguing transport and optical phenomena have already been reported in tellurene, including the quantum Hall effect [6,14], spin Hall effect [15], weak antilocalization [16], chirality-dependent nonlinear magnetotransport [17–22], and THz helicity-sensitive currents [23].

Most recently, the nonlinear Hall effect (NLHE) has been observed in transport measurements on tellurium-based thin flakes and tellurene devices [7,24]. The NLHE is a transverse dc electric current or voltage response that is quadratic in the driving electric field, which appears even in time-reversal-symmetric conditions provided the material lacks inversion symmetry [25–29]. NLHE has been detected in topological insulators, Weyl semimetals, as well as 2D systems like transition metal dichalcogenides, graphene, topological surface states, and others [30–34]. The sun-shaped sample configuration has proven to be the most efficient method of detection [35]. It is commonly emphasized that it is the Berry curvature dipole (BCD) which is responsible for the microscopic origin of NLHE [7,24–36]. At the same time, the BCD is not necessarily the dominant mechanism of NLHE, and other mechanisms, such as side-jump or asymmetric (skew) scattering, may play an essential role [27–29]. This distinction is especially relevant for tellurium-based systems: NLHE in gate-tuned 2D Te has been interpreted in terms of a large BCD near the Weyl band edge [7], whereas room-temperature Te thin flakes have shown a giant NLHE dominated by extrinsic scattering and enabled by symmetry reduction at the surface [24].

Independent of the microscopic origin, the symmetry of the actual system must be stated carefully. In

*Contact author: sergey.ganichev@ur.de

 ©2026 American Physical Society

time-reversal-invariant systems, broken inversion symmetry is a necessary but not sufficient condition for the NLHE: the relevant second order conductivity tensor must also contain symmetry-allowed components under the remaining crystal symmetries [25–29]. In substrate-supported tellurene, the symmetry is as low as C_1, and all in-plane second order coefficients are symmetry-allowed. Consequently, transverse, longitudinal, and diagonal with respect to the electric field second order currents, as well as polarization-independent and helicity-dependent rectification, are not excluded by symmetry [23].

It is important to highlight the connection between the NLHE and the photogalvanic effect in radiation induced high-frequency experiments. The photogalvanic effect represents the generation of a dc electric current under absorption of light in unbiased systems [37–40]. In optical language, the photo-current response to linearly polarized radiation is the linear photogalvanic effect (LPGE), where "linear" refers to the polarization state of the radiation rather than to the order of the response. Under an alternating electric field, the generated LPGE dc current is governed by just the same second order conductivity tensor that underlies low-frequency nonlinear transport response. Consequently, the LPGE current component perpendicular to the exciting ac electric field is the high-frequency counterpart of the NLHE, while its component parallel to the field corresponds to nonlinear longitudinal transport.

Our previous work (Ref. [23]) established THz-driven nonlinear transport in tellurene excited by circularly polarized radiation, emphasizing the helicity-dependent response. In this work, we present the observation and a comprehensive study of THz radiation-driven second order transport in tellurene driven by *linearly* polarized radiation. By varying the relative orientation of the high-frequency electric field and the detected dc photocurrent, we resolve transverse, diagonal, and longitudinal second order responses, including the NLHE. Our theory incorporates both intrinsic and extrinsic microscopic mechanisms of nonlinear current generation, namely the BCD, side-jump, and skew-scattering contributions. Our THz radiation approach offers several experimental advantages: (i) contactless application of the alternating electric field, (ii) straightforward control of the field orientation by a half-wave plate, (iii) direct access to dc longitudinal second order currents without a linear dc background, (iv) implementation of a simple Hall-bar geometry, and (v) operation in a large temperature range up to room temperature.

II. PHENOMENOLOGICAL CONSIDERATION

We begin with the phenomenological theory of the nonlinear transport in tellurene samples. Second order transport phenomena, including the nonlinear Hall currents that are quadratic in the external electric field, can appear even in time-reversal symmetric conditions. The direct current generated in response to a static electric field $\boldsymbol{E}$ is expressed by the following relation:

$$j^{\alpha} = \sigma^{(1)}_{\alpha\mu} E_{\mu} + \sigma^{(2)}_{\alpha\mu\nu} E_{\mu} E_{\nu}. \tag{1}$$

Here $\sigma^{(2)}_{\alpha\mu}$ and $\sigma^{(2)}_{\alpha\mu\nu}$ are the first (linear conductivity) and second (nonlinear conductivity) order in electric field dc conductivity tensors, respectively, and α, μ, and ν run over in-plane Cartesian coordinates. In the high-frequency regime, the first term in Eq. (1) averages to zero and the resulting dc current arises as a second order response to the ac electric field $\boldsymbol{E}_{\omega}(t) = \boldsymbol{E}\exp(-i\omega t) + \boldsymbol{E}^{*}\exp(i\omega t)$. The dc current generated by linearly polarized radiation is sensitive to the orientation of the in-plane electric field and is given by

$$\begin{aligned} j^{\alpha} &= \sigma^{(2)}_{\alpha\mu\nu}(\omega) E_{\mu} E^{*}_{\nu} \\ &= \chi_{\alpha\mu\nu}(\omega)(E_{\mu}E^{*}_{\nu} + E^{*}_{\mu}E_{\nu}), \end{aligned} \tag{2}$$

where $\hat{\boldsymbol{\chi}}(\omega)$ is the third rank tensor. The symmetry of the studied tellurene is reduced to the point group C_1 [23]. In such systems, for excitation with homogeneous radiation at normal incidence, Eq. (2) assumes the form

$$J^{c} = J^{c}_{L1}\cos 2\alpha + J^{c}_{L2}\sin 2\alpha + J^{c}_{0}, \tag{3}$$

$$J^{a} = J^{a}_{L1}\cos 2\alpha + J^{a}_{L2}\sin 2\alpha + J^{a}_{0}. \tag{4}$$

Here $J^{c} \propto |\boldsymbol{E}|^2 \propto P_s$ and $J^{a} \propto |\boldsymbol{E}|^2 \propto P_s$ are currents excited along c and a axes ($a \perp c$), J^{c}_{L1}, J^{a}_{L1} J^{c}_{L2}, J^{a}_{L2}, J^{c}_{0}, and J^{a}_{0} are six linearly-independent current contributions which, due to the absence of any nontrivial symmetry operation, are not related to one another; P_s is the radiation power, and the azimuth angle α defines the orientation of the electric field with respect to the c axis.

III. DEVICES AND EXPERIMENTAL TECHNIQUE

Experiments on THz nonlinear transport in tellurene samples were performed on Hall bar samples with a long side oriented along the c axis. A high-frequency electric field was applied to the sample via contactless normal-incident irradiation using a monochromatic THz laser, with frequencies ranging from 0.6 to 2.54 THz. DC electric current caused by the nonlinear transport effects was measured along the c axis (source-drain contacts) and a axis (contacts 2 and 6 on the opposite sides of the Hall bar), see Figs. 1(a) and 1(e). The Te flakes were fabricated using a hydrothermal growth process similar to that previously reported for growing tellurene nanofilms [6,23]. The synthesized 2D Te flakes had a thickness of approximately 30 nm. The as-grown 2D Te films were first cleaned twice with deionized water and then dispersed onto a 90 nm SiO_2/525 μm p+Si substrate using the Langmuir-Blodgett method [41]. Hall-bar devices were patterned using electron beam lithography, and 50 nm Ni metal contacts were deposited by electron beam evaporation at a pressure below 2×10^{-6} Torr. Figures 1(a) and 1(b) show the photograph and cross-section of the studied devices, respectively. The source and drain contact distance is about 40 μm. The substrate served as a back gate, which allowed us to change the concentration and carrier type. We studied two samples (A and B) with close parameters. Sweeping the gate voltage U shows the charge neutrality point (CNP), see Figs. 1(c) and 1(d). At room temperature, the CNP is detected at large negative gate voltages, $U \approx -12$ V for sample A and $U \approx -10$ V for sample B. Thus, for convenience, we use here and below an effective gate voltage $U_{\mathrm{G}} = U - U_{\mathrm{CNP}}$, where U_{CNP} is the voltage at which the CNP appears. For positive and negative U_{G}, we have electron and hole-type conductivity, respectively [42]. For low temperatures, the CNP is at about

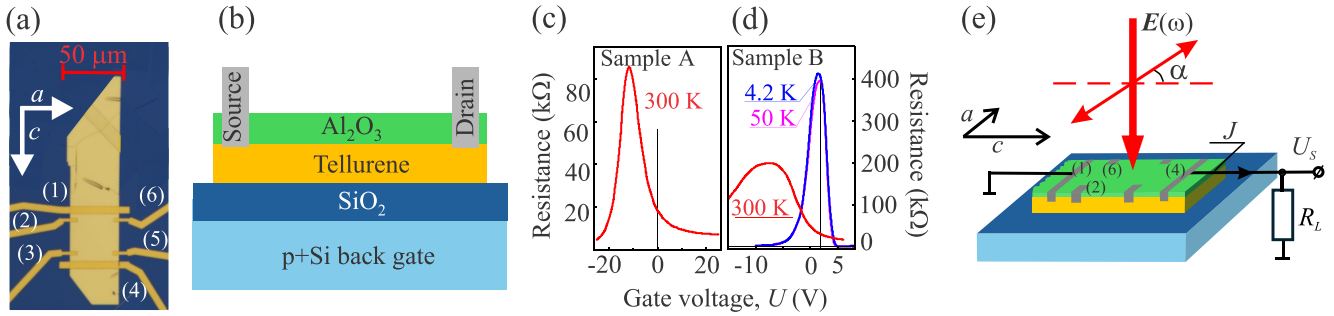


FIG. 1. (a) and (b) show an optical micrograph of sample A and a cross-section of the samples. The tellurene flake is deposited on top of p+Si substrate covered by a 90 nm SiO_2 layer. Nickel source and drain contacts with thickness of 50 nm are fabricated by electron beam evaporation on the short sides of the tellurene flakes, which were 38×41 μm^2. Te flakes are capped by a 15-nm-thick layer of Al_2O_3. (c) and (d) show the two-point resistance measured along the c axis as a function of the back gate voltage for samples A and B, respectively. (e) sketches the experimental setup. The azimuth angle α defines the orientation of the radiation electric field vector $\boldsymbol{E}$ with respect to the c axis.

1 V. For gate voltages above approximately 3 V, the resistance decreases rapidly with increasing gate voltage. Since the rapid decrease in resistance for $U_G > 3$ V represents a deviation from the behavior expected in the regime of interest, we focus our study of the photocurrent at low temperatures on gate voltages below 3 V. Figure 1(d) shows that cooling the sample results in a shift of the CNP position. Since tellurene is a narrow bandgap semiconductor, at room temperature the CNP is strongly related to interface traps, dielectric charges, thermally activated holes and electrons, their mobility and the contact resistance. Cooling down will then result in a shift in CNP. Indeed, the gate voltage corresponding to charge neutrality is affected by temperature-dependent electrostatic charging/trapping, temperature dependence of the carrier density, and interfacial trap state freezing. In a low-dimensional device with dielectric interfaces, even a relatively small change in trapped charge can result in a sizable shift of the apparent CNP. We therefore interpret the observed shift primarily as a change of the electrostatic offset rather than as a large intrinsic displacement of the band structure. The carrier concentration for an effective gate voltage of ±20 V is about 5×10^{12} cm^{-2}, and the room temperature mobility μ is about 430 and 170 cm^2/Vs for holes and electrons, respectively.

Pulsed and continuous wave (cw) line-tunable molecular THz lasers optically pumped by CO_2 lasers were used as sources of THz electric field. The pulsed NH_3 laser [43] pumped by a transversely excited atmosphere (TEA) CO_2 laser operated at frequencies $f = 0.60$, 1.07, and 2.02 THz ($\hbar\omega = 2.5$, 4.4 and 8.35 meV). The pulsed laser generated single pulses at a repetition rate of 1 Hz, with a pulse duration of approximately 100 ns. The laser's peak power and pulse shape were controlled by the THz photon drag detector [44]. Maximum peak powers P were about 20 kW (2.02 THz), 5 kW (1.07 THz), and 1.5 kW (0.6 THz). The cw CH_3OH laser operated at a frequency of 2.54 THz ($\hbar\omega = 10.5$ meV). The radiation with the power P in the range from 5 to 30 mW was modulated by an optical chopper operating at a frequency of about 80 Hz. The samples were exposed to linearly polarized radiation with normal incidence, see Fig. 1(e), and the radiation induces indirect optical transitions (Drude-like free-carrier absorption) in the lowest subband.

Most experiments were performed at room temperature. To test the influence of temperature reduction, several experiments were also performed at 50 and 4.2 K. For room temperature, we used a 90° off-axis parabolic mirror with the focal plane of 75 mm. For low temperature measurements, the samples were placed in a temperature controllable optical cryostat with z-cut quartz and TPX (4-methyl-1-pentene) windows. In this case, the off-axis mirror focal plane was 170 mm. In order to block visible and near-infrared radiation, the windows were additionally covered by black polyethylene foil. The beam shape and parameters were controlled using a pyroelectric camera [43,45]. The pulsed laser spot diameters at FWHM varied from 2.6 to 3.1 mm depending on the radiation frequency. For cw laser radiation, it was 0.9 mm. Considering the area of the devices, S_{device}, we obtain the power irradiating the sample $P_s = P\times(S_{\text{device}}/S_{\text{spot}})$, where P is the radiation power, and S_{spot} is the beam spot area. The orientation of the electric field with respect to the c axis is defined by an azimuth angle, α, as shown in the inset of Fig. 1(e). The angle α was controllably varied by rotating half-wave plates or by placing a grid wire behind a quarter-wave plate set. The radiation power dependencies were obtained using the cross-polarizer technique, which employs two wire grid polarizers. The first polarizer was rotated to modify the radiation power, while the second polarizer remained fixed to ensure an unchanged output polarization [46,47].

In the setup with the pulsed laser, the induced photocurrent was detected as a voltage drop V_{ph} across load resistors $R_{\text{L}} = 50$ Ohm. The signals were amplified by a voltage amplifier with a gain of $k = 100$ and a bandwidth of 300 MHz and recorded by a digital broad band (1 GHz) oscilloscope. The photocurrent is obtained as $J = V_{\text{ph}}/(kR_{\parallel})$, where $R_{\parallel} = (R_{\text{s}}\times R_L)/(R_{\text{s}} + R_L)$ and R_{s} is the sample resistance. In the cw laser setup, the photovoltage signals V_{ph} were measured by modulating the incoming radiation with an optical chopper and using a standard lock-in technique. The resulting signal is related to the photocurrent as $J = V_{\text{ph}}/(k_{\text{a}}R_{\text{s}})$, where k_{a} is the preamplifier gain coefficient.

IV. RESULTS

First, we present the results obtained at room temperature when applying the pulsed laser. Figure 2(a) shows the dependence of the dc current J^c generated along the c axis in sample A by the ac electric field with frequency $f = 2.02$

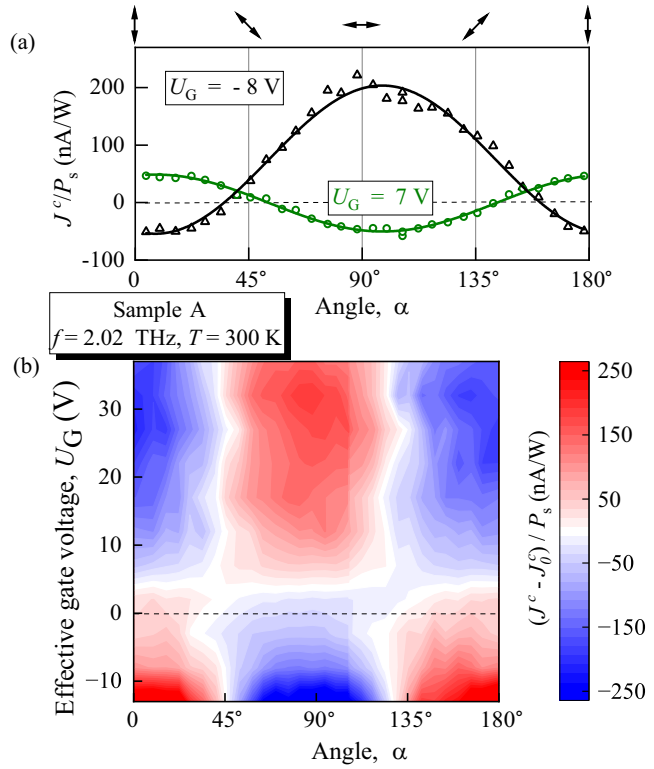


FIG. 2. (a) Azimuth angle dependence of the photocurrent J normalized to the power P_s excited by radiation with $f = 2.02$ THz. The data are shown for sample A at room temperature and two effective back gate voltages $U_G = -8$ V and 7 V. Solid lines are fits after Eq. (3). Double arrows on top show orientations of the electric field vector for several angles α. (b) Azimuth angle and effective gate voltage dependence of the photocurrent $(J^c - J_0^c)/P_s$ excited in sample A by radiation with $f = 2.02$ THz, where J_0 is the polarization independent offset. The effective gate ranges from negative (hole-conductivity) to positive values (electron-conductivity).

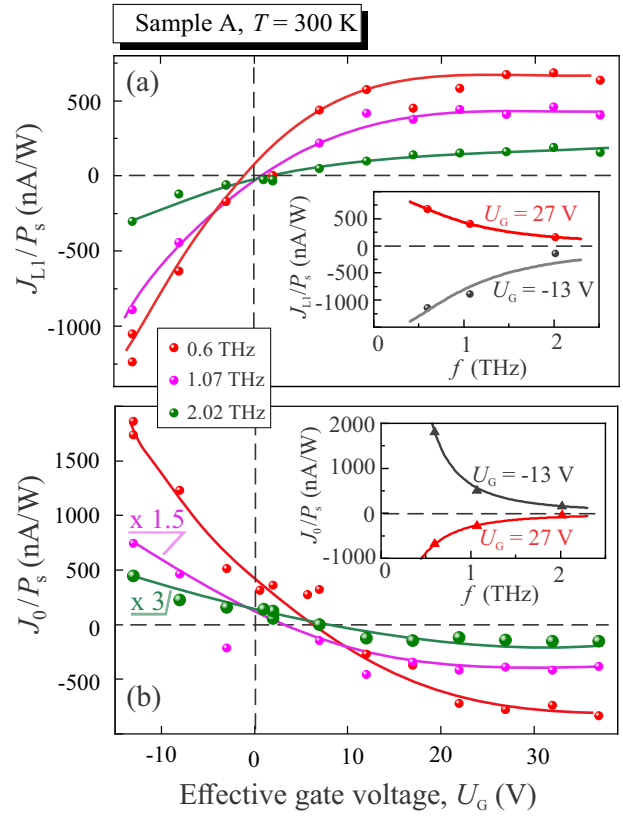


FIG. 3. Effective gate voltage dependencies of the fitting parameters J_{L1} (a) and J_0 (b). The data are obtained for sample A excited by radiation at three frequencies. The insets show frequency dependencies of J_{L1} and J_0 for several values of positive and negative effective gate voltages. Solid lines are guides for the eye.

THz. For positive effective gate voltages (circles), the current is excited in the conduction band and for the negative U_G in the valence band. The polarization dependence is well described by Eq. (3). The fit reveals that the signal is dominated by the first ($\propto J_{L1}^c$) and last terms ($\propto J_0^c$) of Eq. (3). Figure 2(b) shows a color map of the polarization dependent current contribution $J^c - J_0^c$ as a function of the azimuth angle α and effective gate voltage U_G. The figure shows that, for all gate voltages, the polarization dependence of the current in sample A is determined by the first term of Eq. (3). The same result has been obtained for lower frequencies 1.07 and 0.6 THz. Figures 3(a) and 3(b) show the gate voltage dependencies of J_{L1}^c and J_0^c contributions obtained for three radiation frequencies. These figures show that the magnitudes of both contributions increase with decreasing frequency. This tendency is shown in the insets in Fig. 3 for two values of effective gate voltages ($U_G = -13$ and 27 V). Figure 4 shows the dependence of the total current J^c on the electric field square obtained for frequencies $f = 1.07$ and 2.02 THz, and two gate voltages $U_G = -13$ and 37 V. The data confirm that, in agreement with Eq. (3), the current scales linearly with the radiation intensity $I = P/S_{spot} \propto E^2$.

While in sample A at room temperature the current J^c is dominated by the contributions proportional to the coefficients J_{L1}^c and J_0^c in Eq. (3) and the current defined by the coefficient J_{L2}^c is negligible, in sample B, the latter one becomes essential for both positive and negative effective gate voltages. Figures 5(a)–5(e) show the azimuth angle dependencies obtained for sample B excited by low power radiation of a cw laser with frequency 2.54 THz. The data are presented for several gate voltages. The data are well fitted by Eq. (3), see solid lines in panels (a)–(e). Azimuth angle dependencies of the individual contributions proportional to the coefficients J_{L1}^c, J_{L2}^c and J_0^c, which were used for the fits, are shown by dashed, dot-dashed and dotted lines, respectively. It is seen that for some effective gate voltages the contribution $\propto J_{L2}^c$ is substantial and can even dominate, see, e.g., Fig. 5(c).

The current is also detected in the direction a perpendicular to the c axis, see Figs. 6(a)–6(c). It is seen that the current magnitudes for these two directions are very close to each other. We also note that for this direction the contribution $\propto J_{L2}^c$ varying as $\sin(2\alpha)$ is dominating for positive effective gate voltages.

All data presented so far have been obtained in samples at room temperature. Cooling down the tellurene devices results in a substantial (by two orders of magnitude) increase of the current magnitude. Figures 7(a)–7(f) show the data obtained in sample B for temperatures 50 and 4.2 K and radiation

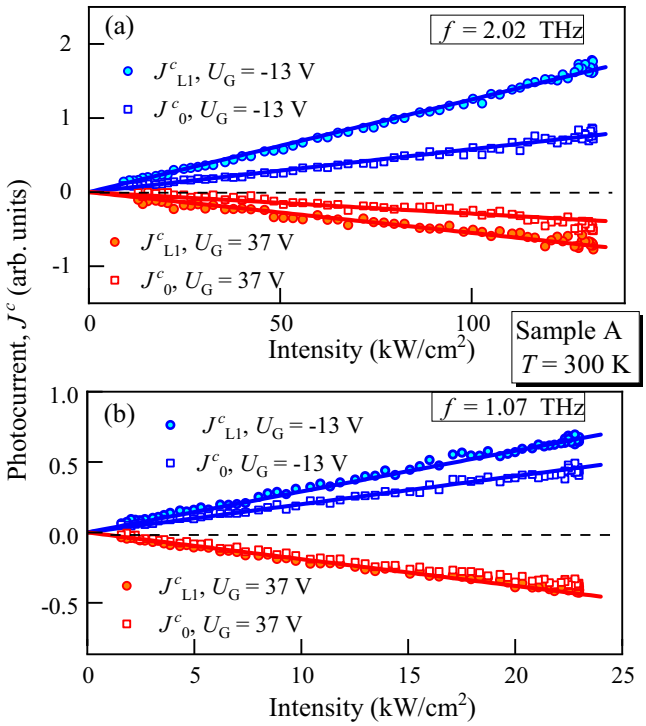


FIG. 4. Dependencies of the photocurrent J on the radiation intensity $I = P/S \propto E^2$. The data are obtained for frequencies $f = 2.02$ (top) and 1.07 THz (bottom) and several effective gate voltages. Solid lines show fits after $J \propto E^2$.

frequency 2.54 THz (low power cw laser). As at room temperature, see Fig. 5, the data can be well fitted by Eq. (3) with comparable magnitude of all contributions.

V. MICROSCOPIC THEORY

As shown above, the functional dependencies of the current excited by THz radiation can be well described by the phenomenological theory of second order transport phenomena. In agreement with Eqs. (3) and (4), the current scales as the square of the radiation electric field and varies with the azimuth angle as a sum of $\cos(2\alpha)$ and $\sin(2\alpha)$, and has a polarization-independent contribution, see Figs. 2, 4, 5, and 7. This behavior is observed in directions both along and perpendicular to the c axis, see Fig. 5. Together with the fact that the current is detected at normal incidence, these observations confirm the reduction of symmetry compared to bulk Te, and indicate that the symmetry of the studied tellurene is C_1, ruling out any nontrivial symmetry elements. Analyzing the current behavior in relation to variations in microscopic parameters such as gate voltage and radiation frequency requires a microscopic theory of nonlinear transport, which is provided below.

The investigated LPGE currents are excited by THz radiation with a photon energy of a few meV, which is lower than the energy gap of tellurene. The typical carrier energies also exceed the photon energy. Consequently, LPGE is caused by the free carrier Drude-like radiation absorption in the conduction or valence band. Therefore a theoretical description of the photocurrents is performed in the semiclassical picture in which the THz radiation acts on the carriers as an ac electric field [23,48,49]

$$\boldsymbol{E}_\omega(t) = \boldsymbol{E}\exp(-i\omega t) + \text{c.c.} \tag{5}$$

In the semiclassical theory, transport is described by the Boltzmann kinetic equation for the electron distribution function $f_{\boldsymbol{k}}$. Here $\boldsymbol{k}$ is the two-dimensional electron wave vector, and the equation has the following form

$$\frac{\partial f_{\boldsymbol{k}}}{\partial t} + \frac{q}{\hbar}\boldsymbol{E}_\omega(t)\cdot\frac{\partial f_{\boldsymbol{k}}}{\partial \boldsymbol{k}} = \sum_{\boldsymbol{k}'}(W_{\boldsymbol{k}\boldsymbol{k}'}f_{\boldsymbol{k}'} - W_{\boldsymbol{k}'\boldsymbol{k}}f_{\boldsymbol{k}}), \tag{6}$$

where $W_{\boldsymbol{k}'\boldsymbol{k}}$ is the probability of $\boldsymbol{k}' \leftarrow \boldsymbol{k}$ electron scattering, and q is the carrier charge, equal to $\pm|e|$ for holes and electrons, respectively. The electric current density $\boldsymbol{j}$ is calculated as

$$\boldsymbol{j} = g_s g_v q \sum_{\boldsymbol{k}} f_{\boldsymbol{k}}\boldsymbol{v}_{\boldsymbol{k}}, \tag{7}$$

where g_s and $g_v = 2$ are the spin and valley degeneracies, and $\boldsymbol{v}_{\boldsymbol{k}}$ is the carrier velocity. For electrons and holes in tellurene we have $g_s = 2$ and $g_s = 1$, respectively.

There are three microscopic mechanisms of THz radiation-induced photocurrents. These are the extrinsic contributions due to skew scattering processes and side jumps, as well as the intrinsic Berry curvature dipole mechanism [27–29,50,51]. These mechanisms completely exhaust the photocurrent driven by circular polarization, as proven by a comparison with the results of a rigorous quantum-mechanical calculation [51]–at least in gapped systems. However, the gapless Weyl semimetals require further investigation [52].

First we consider the skew-scattering contribution. The generation process of the skew-scattering induced LPGE can be illustrated as follows. At linear polarization of THz radiation, an alignment of electron momenta takes place: there is a larger number of particles with momenta along and opposite to the electric field direction and a smaller number in the perpendicular direction. The corresponding stationary momentum distribution is shown in Fig. 8 (left panels) by green color. Due to low (C_1) symmetry of the tellurene sample, scattering of 2D carriers occurs by asymmetrical defects. Scattering of the momentum-aligned carriers (dashed arrows) by such defects results in uncompensated charge flows (solid arrows) and in a dc electric current (red arrows). The photocurrent is shown for holes; it reverses its direction for electrons.

Microscopically, the photocurrent, being a second order dc response, is given by the correction to the distribution function obtained by two iterations of the kinetic Eq. (6) in powers of the electric field $\boldsymbol{E}$. In this approach, the distribution function is sought in the form

$$f_{\boldsymbol{k}} = f_0 + [f_1\exp(-i\omega t) + \text{c.c.}] + f_2, \tag{8}$$

where f_0 is the equilibrium distribution at $E = 0$, $f_1 \propto E$ is a linear correction, and $f_2 \propto E^2$ is a dc contribution quadratic in E. Double iteration of the Boltzmann kinetic Eq. (6) in the electric field amplitude $\boldsymbol{E}_\omega(t)$ yields the stationary correction to the charge-carrier distribution function $f_2(\boldsymbol{k})$ describing an alignment of their momenta. The alignment means a larger number of carriers with momenta along $\pm\boldsymbol{E}_\omega$ direction than

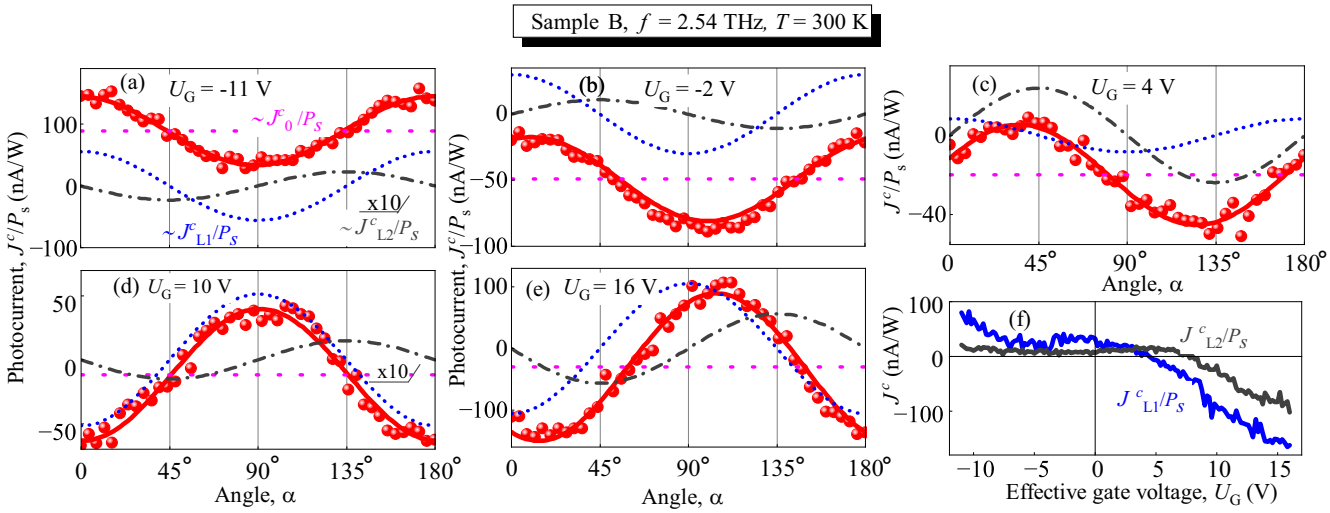


FIG. 5. [(a)–(e)] Dependencies of the normalized photocurrent J^c/P_s (red circles) on the azimuth angle α measured in sample B. The data are obtained for $f = 2.54$ THz, room temperature, and for several effective back gate voltages ranging from hole ($U_G < 0$) to electron conductivity ($U_G > 0$). The magnitudes of the currents J^c_{L2} in (a) and (d) are multiplied by a factor of 10 for visibility. Red solid lines are fits after Eq. (3). The azimuth angle dependencies of the individual current contributions J^c_{L1}, J^c_{L2}, and J^c_0 are plotted by the blue dotted, dark gray dot-dashed, and magenta dashed lines, respectively. (f) Current contributions J^c_{L1}, and J^c_{L2} as a function of the effective gate voltage.

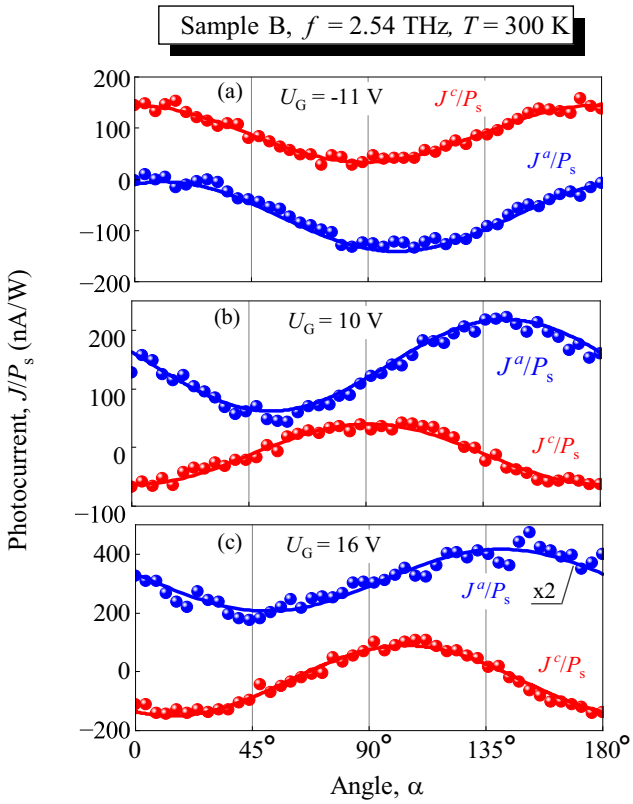


FIG. 6. Dependencies of the normalized photocurrent J^c/P_s (red circles) and J^a/P_s (blue circles) on the azimuth angle α measured in sample B. The data are obtained for $f = 2.54$ THz, room temperature, and for several effective back gate voltages ranging from hole ($U_G < 0$) to electron conductivity ($U_G > 0$). The magnitudes of current J^a/P_s in panel (c) are multiplied by a factor of 2 for visibility. Red and blue solid lines are fits after Eqs. (3) and (4), respectively.

perpendicular to it. The dc part of the distribution function, $f_0 + f_2$, is shown by green color in Fig. 8.

Momentum alignment does not describe an electric current because the corresponding distribution is even in $\boldsymbol{k}$. In order to obtain a part of the distribution that is odd in momentum, we take into account the skew scattering.

In low symmetry systems, the scattering probability in the kinetic Eq. (6) does not satisfy the principle of detailed balance: the probability of the $\boldsymbol{k} \leftarrow \boldsymbol{k}'$ process, $W_{\boldsymbol{k}\boldsymbol{k}'}$ differs from that of the inverse process, $W_{\boldsymbol{k}'\boldsymbol{k}}$. Therefore it is convenient to split it into the symmetric and asymmetric parts: $W_{\boldsymbol{k}\boldsymbol{k}'} = W^s_{\boldsymbol{k}\boldsymbol{k}'} + W^a_{\boldsymbol{k}\boldsymbol{k}'}$, where $W^{s,a}_{\boldsymbol{k}\boldsymbol{k}'} = \pm W^{s,a}_{\boldsymbol{k}'\boldsymbol{k}}$. The asymmetric part $W^a_{\boldsymbol{k}\boldsymbol{k}'}$ is nonzero in systems of C_1 symmetry [49] and is responsible for the skew scattering. Here, "skew scattering" refers to the asymmetric part of the charge-carrier scattering probability and does not involve spin or valley degrees of freedom. We use the term in this conventional transport-theory sense [29,51,53–57].

The symmetrical part of the scattering probability $W^s_{\boldsymbol{k}\boldsymbol{k}'}$ defines the relaxation times of different Fourier harmonics of the distribution function. In particular, we introduce the times $\tau_{1,2}$ dependent on the carrier's energy ε_k defined as follows [48]:

$$\tau_n^{-1}(\varepsilon_k) = \sum_{\boldsymbol{k}'} W^s_{\boldsymbol{k}\boldsymbol{k}'}(1 - \cos n\theta_{\boldsymbol{k}\boldsymbol{k}'}), \tag{9}$$

where $\theta_{\boldsymbol{k}\boldsymbol{k}'}$ is the scattering angle. At ε_k equal to the Fermi energy ε_F, they give the transport scattering time, which determines the mobility, $\tau_{tr} = \tau_1(\varepsilon_F)$ and the alignment relaxation time $\tau_{al} = \tau_2(\varepsilon_F)$.

The momentum-aligned carriers are scattered by asymmetrical defects predominantly in the same direction, Fig. 8, which means a net electric current. The current is microscopically calculated by taking into account $W^a_{\boldsymbol{k}\boldsymbol{k}'}$ in the lowest

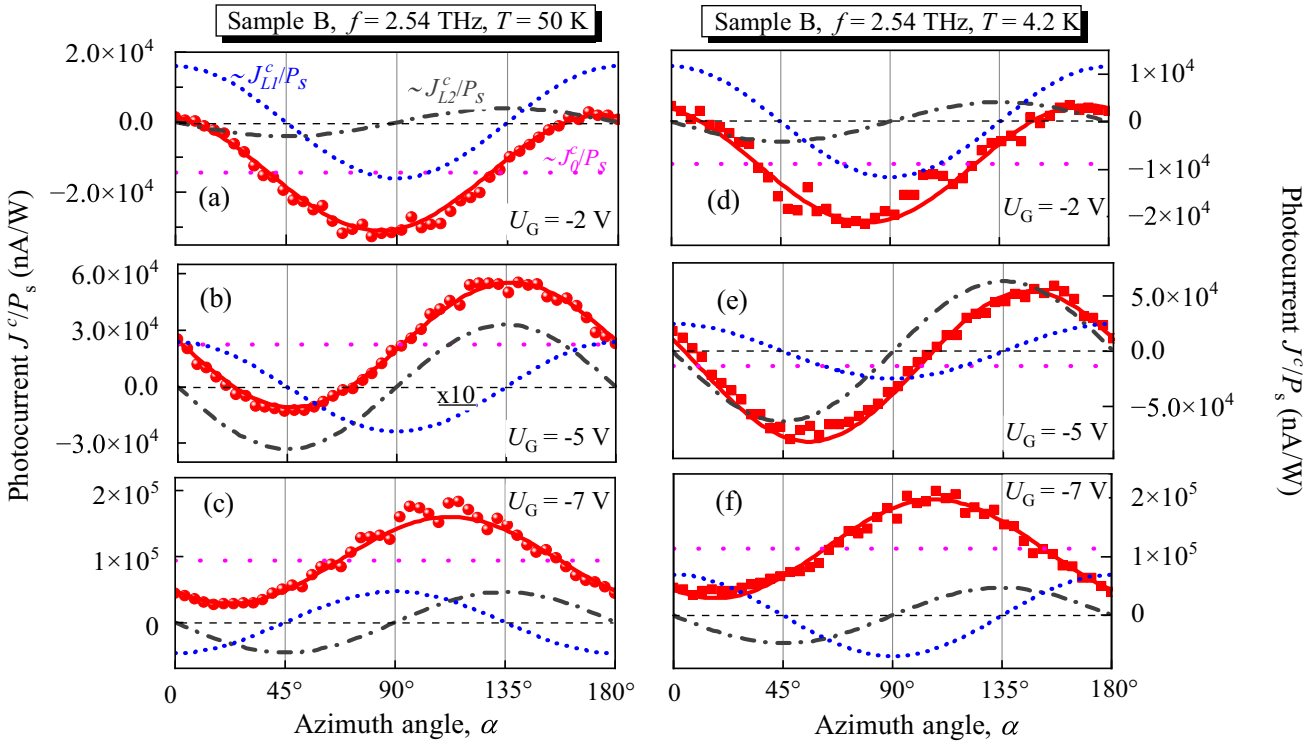


FIG. 7. Dependencies of the normalized photocurrent J^c/P_s (circles) on the azimuth angle α measured in sample B for the source-drain pair of contacts and several effective back gate voltages. The data are obtained for $f = 2.54$ THz and two temperatures 50 K [(a)–(c)] and 4.2 K [(d)–(f)]. The magnitudes of the currents J^c_{L2} in (b) are multiplied by a factor of 10 for visibility. Solid lines are fits after Eq. (3). The azimuth angle dependencies of the individual current contributions J^c_{L1}, J^c_{L2}, and J^c_0 are plotted by the blue dotted, dark gray dot-dashed, and magenta dashed lines, respectively.

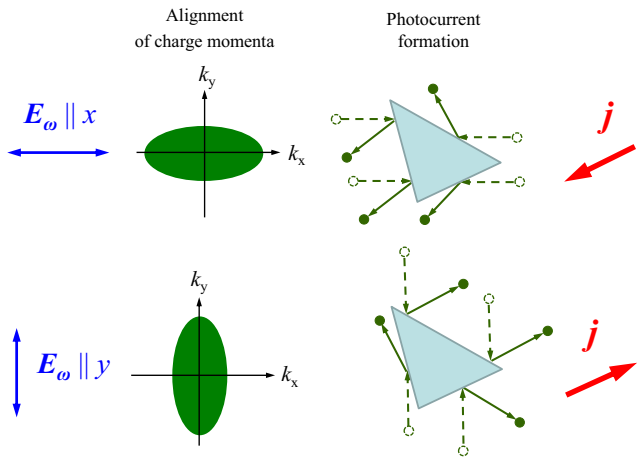


FIG. 8. Microscopic mechanism of the photocurrent formation. Under linearly polarized THz excitation, the carrier momentum distribution becomes anisotropic: the number of particles with momenta aligned parallel or antiparallel to the electric field exceeds that of carriers with transverse momenta. The corresponding stationary momentum distribution is shown in green. Scattering of these momentum-aligned carriers (dashed arrows) by irregular triangles results in uncompensated charge flows (solid arrows) and in a dc electric current (red arrows). The photocurrent is shown for holes; it reverses its direction for electrons.

order. The corresponding dc correction to the distribution function, f^a_2, yields the current density by Eq. (7) with the band velocity

$$\boldsymbol{v}^{\rm band}_{\boldsymbol{k}} = \frac{1}{\hbar}\nabla_{\boldsymbol{k}}\varepsilon_k. \tag{10}$$

The LPGE current density driven by linear polarization of radiation reads

$$j_{c,a} = |\boldsymbol{E}|^2 e v_{\rm F}\sigma(\omega)\Bigg\{2\frac{\left[v_{\rm F}^3\tau_{\rm al}(\Xi_{c,s}P_{\rm L1}+\Lambda_{c,s}P_{\rm L2})\right]'}{v_{\rm F}^3} - \frac{\tau_{\rm al}}{\tau_{\rm tr}} \times \tau'_{\rm tr}\frac{1-\omega^2\tau_{\rm tr}\tau_{\rm al}}{1+\omega^2\tau_{\rm al}^2}[(\Xi_{c,s}\mp\Lambda_{s,c})P_{\rm L1}\mp(\Xi_{s,c}\pm\Lambda_{c,s})P_{\rm L2}]\Bigg\}. \tag{11}$$

Here $\sigma(\omega) = \sigma_0/(1+\omega^2\tau_{\rm tr}^2)$ is the frequency-dependent conductivity with σ_0 being the dc conductivity,

$$P_{\rm L1} = \frac{|E_c|^2 - |E_a|^2}{|\boldsymbol{E}|^2}, \quad P_{\rm L2} = \frac{2{\rm Re}(E_c E_a^*)}{|\boldsymbol{E}|^2} \tag{12}$$

are the Stokes parameters describing the linear polarization degree of radiation, the prime denotes the derivative with respect to the Fermi energy, and $v_{\rm F}$ is the Fermi velocity. We assumed a parabolic energy dispersion and degenerate statistics. The asymmetry of the scattering probability present in

the C_1 point group is taken into account by the dimensionless factors $\Xi_{c,s}$, $\Lambda_{c,s} \ll 1$ defined as follows:

$$\Xi_{c(s)} = \tau_{\rm tr} \sum_{\boldsymbol{k}'} \left\langle \cos\,(2\varphi_{\boldsymbol{k}}) W^a_{\boldsymbol{k}'\boldsymbol{k}} \cos(\sin)\varphi_{\boldsymbol{k}'} \right\rangle,$$
$$\Lambda_{c(s)} = \tau_{\rm tr} \sum_{\boldsymbol{k}'} \left\langle \sin\,(2\varphi_{\boldsymbol{k}}) W^a_{\boldsymbol{k}'\boldsymbol{k}} \cos(\sin)\varphi_{\boldsymbol{k}'} \right\rangle, \tag{13}$$

where the brackets denote averaging over the directions of $\boldsymbol{k}$ at the Fermi circle, and the polar angles are measured from the c axis.

There are two terms in the skew scattering probability resulting in the LPGE current contributions depending differently on the density of scatterers. A so-called conventional skew scattering occurs with non-Gaussian disorder and appears in the third order in the scattering potential. It is present at low temperatures for scattering by impurities, but is absent for acoustic phonon scattering when single-phonon processes are dominant [58,59]. The corresponding contribution to the skew scattering probability contains the density of defects $\mathcal{N}_d$, therefore $\Xi_{c,s}$ and $\Lambda_{c,s}$ are independent of $\mathcal{N}_d$, and the LPGE current $j \propto 1/\tau \propto \mathcal{N}_d$ at $\omega\tau \gg 1$. Another, the so-called intrinsic (or coherent) skew scattering, occurs at any potential [60–62]. The intrinsic skew scattering probability is proportional to the fourth power of the disorder potential and to $\mathcal{N}_d^2$. It gives a contribution to LPGE which scales quadratically with the scattering rates and $\mathcal{N}_d$ at high frequencies: $j \propto \mathcal{N}_d/\tau \propto \mathcal{N}_d^2$. For scattering by phonons, $\mathcal{N}_d$ is substituted by the temperature [58].

We note that, in contrast to the intraband photocurrent driven by circular polarization, where the skew scattering gives a small contribution at $\omega\tau \gg 1$ [51], the LPGE current can be effectively generated due to this extrinsic mechanism at all frequencies, and can even be dominant.

There is another mechanism of LPGE which is related to the Berry curvature of carriers in the conduction and valence bands of tellurene. In the semiclassical approach, the Berry curvature dipole (BCD) mechanism of LPGE is accounted for in the anomalous velocity linear in the radiation electric field and oscillating in time with the frequency ω:

$$\boldsymbol{v}^{\rm anom}_{\boldsymbol{k}}(t) = \boldsymbol{\Omega}_{\boldsymbol{k}} \times \boldsymbol{E}_\omega(t). \tag{14}$$

Here the Berry curvature reads $\boldsymbol{\Omega}_{\boldsymbol{k}} = \boldsymbol{\nabla}_{\boldsymbol{k}} \times i\langle u_{\boldsymbol{k}}|\nabla_{\boldsymbol{k}} u_{\boldsymbol{k}}\rangle$, with $u_{\boldsymbol{k}}$ being the electron Bloch amplitude for the energy band where the radiation is absorbed. Finding the linear correction to the distribution function $f_1 \propto E_\omega(t)$ from the Boltzmann Eq. (6) with the symmetrical part of the scattering probability $W^s_{\boldsymbol{k}'\boldsymbol{k}}$ only, the BCD contribution to the LPGE current is then calculated by Eq. (7) with $\boldsymbol{v}_{\boldsymbol{k}} = \boldsymbol{v}^{\rm anom}_{\boldsymbol{k}}(t)$. The corresponding dc current density reads [50]

$$\boldsymbol{j}^{\rm BCD} = -\frac{2q^3\tau}{1+\omega^2\tau^2}[\hat{\boldsymbol{z}} \times \boldsymbol{E}](\boldsymbol{D} \cdot \boldsymbol{E}). \tag{15}$$

Here $\boldsymbol{D}$ is the Berry curvature dipole introduced in Ref. [25]:

$$\boldsymbol{D} = \frac{2g_s g_v}{\hbar^2} {\rm Im} \sum_{\boldsymbol{k}} f_0(\varepsilon_{\boldsymbol{k}}) \boldsymbol{\nabla}_{\boldsymbol{k}} \langle \partial_{k_x} u_{\boldsymbol{k}} | \partial_{k_y} u_{\boldsymbol{k}} \rangle. \tag{16}$$

Finally, there are contributions to LPGE caused by side jumps of carrier wave packets occurring at momentum scattering [50]. The side-jump $\boldsymbol{r}_{\boldsymbol{k}'\boldsymbol{k}}$ for the scattering process $\boldsymbol{k}' \leftarrow \boldsymbol{k}$ is given by

$$\boldsymbol{r}_{\boldsymbol{k}'\boldsymbol{k}} = -(\boldsymbol{\nabla}_{\boldsymbol{k}'} + \boldsymbol{\nabla}_{\boldsymbol{k}})\Phi_{\boldsymbol{k}'\boldsymbol{k}} + \boldsymbol{A}_{\boldsymbol{k}'} - \boldsymbol{A}_{\boldsymbol{k}}, \tag{17}$$

where $\Phi_{\boldsymbol{k}'\boldsymbol{k}}$ is the phase of the matrix element of scattering $U_{\boldsymbol{k}'\boldsymbol{k}}$, and the Berry connection $\boldsymbol{A}_{\boldsymbol{k}} = i\langle u_{\boldsymbol{k}}|\nabla_{\boldsymbol{k}} u_{\boldsymbol{k}}\rangle$.

The first contribution comes from the side-jump accumulation resulting in the scattering-induced correction to the velocity:

$$\boldsymbol{v}^{\rm sj}_{\boldsymbol{k}} = \sum_{\boldsymbol{k}'} W^s_{\boldsymbol{k}'\boldsymbol{k}} \boldsymbol{r}_{\boldsymbol{k}'\boldsymbol{k}}. \tag{18}$$

Then finding the correction to the distribution function $f_2 \propto E^2$ from the Boltzmann Eq. (6) with the scattering probability $W^s_{\boldsymbol{k}'\boldsymbol{k}}$, the side-jump accumulation contribution to the current is calculated by Eq. (7) with $\boldsymbol{v}_{\boldsymbol{k}} = \boldsymbol{v}^{\rm sj}_{\boldsymbol{k}}$. This contribution to the LPGE current is comparable to the BCD one. Note that the side-jump accumulation is insensitive to the radiation helicity and, hence, does not contribute to the circular polarization-driven current.

The second correction to the distribution function caused by side jumps comes from the linear in the electric field scattering probability $W^{\rm sj}_{\boldsymbol{k}'\boldsymbol{k}}(t)$:

$$W^{\rm sj}_{\boldsymbol{k}'\boldsymbol{k}} = \frac{2\pi}{\hbar} \mathcal{N}_d |U_{\boldsymbol{k}'\boldsymbol{k}}|^2 (e\boldsymbol{E}_\omega \cdot \boldsymbol{r}_{\boldsymbol{k}'\boldsymbol{k}}) \partial_{\varepsilon_{\boldsymbol{k}}} \delta(\varepsilon_{\boldsymbol{k}} - \varepsilon_{\boldsymbol{k}'}). \tag{19}$$

It can be interpreted as a correction to the energy conservation law $\delta(\varepsilon_{\boldsymbol{k}} + e\boldsymbol{E}_\omega \cdot \boldsymbol{r}_{\boldsymbol{k}'\boldsymbol{k}} - \varepsilon_{\boldsymbol{k}'}) - \delta(\varepsilon_{\boldsymbol{k}} - \varepsilon_{\boldsymbol{k}'})$ due to the work of the field during the side jump [63]. Iterating the kinetic Eq. (6) with $W_{\boldsymbol{k}'\boldsymbol{k}} = W^s_{\boldsymbol{k}'\boldsymbol{k}} + W^{\rm sj}_{\boldsymbol{k}'\boldsymbol{k}}(t)$ in $\boldsymbol{E}_\omega(t)$, one finds the so-called anomalous distribution $f^{\rm adist} \propto E^2$, which is time-independent and already odd in $\boldsymbol{k}$. Then the corresponding contribution to the LPGE current is calculated by Eq. (7) with $f_{\boldsymbol{k}} = f^{\rm adist}$ and the band velocity $\boldsymbol{v}^{\rm band}_{\boldsymbol{k}}$ given by Eq. (10).

Comparing the conventional skew-scattering, coherent skew-scattering, BCD, and side-jump contributions to the LPGE current, we see that the first one given by Eq. (11) is different from the others which have the same order of magnitude. The ratio of the currents in (11) and (15) can be estimated as [58,59]

$$\frac{j^{\rm skew}}{j^{\rm BCD}} \sim \frac{\varepsilon_{\rm F}}{\mathcal{N}_d |U_{\boldsymbol{k}'\boldsymbol{k}}|}. \tag{20}$$

The Fermi energy at the highest gate voltages applied is $\varepsilon_{\rm F} \approx 50$ meV. The transport relaxation time is related to $\mathcal{N}_d$ and $|U_{\boldsymbol{k}'\boldsymbol{k}}|$ by $\tau_{\rm tr} = \hbar^3/(m\mathcal{N}_d|U_{\boldsymbol{k}'\boldsymbol{k}}|^2)$, where m is the effective mass. The effective masses for electrons and holes are $m_e = 0.11\, m_0$ and $m_h \approx 0.18\, m_0$, where m_0 is the free electron mass [64]. Using these values and mobilities, we estimate the ratio in Eq. (20) to be between 2.4 and 24 for electrons and between 6.3 and 63 for holes, for a density of scatterers $\mathcal{N}_d$ ranging from 10^{10} to 10^{12} cm^{-2}. This shows that the skew-scattering mechanism dominates for both electrons and holes.

The high-frequency asymptotics $j \propto 1/\omega^2$ is a feature common for all microscopic mechanisms, see Eqs. (11) and (15). Analysis of Eqs. (11) and (13) shows that the LPGE current is an increasing function of the Fermi energy. Therefore the current amplitude should increase with increasing electron

and hole densities, i.e., with the absolute value of the gate voltage.

VI. DISCUSSION

Sections IV and V show that exciting tellurene with terahertz radiation results in the photogalvanic effect, which belongs to the class of second order transport phenomena. Previous studies in Ref. [65] examined linear and circular photogalvanic effects in bulk *p*-type tellurium crystals, revealing a variety of photocurrent origins depending on the type of optical transitions responsible for radiation absorption, polarization state, external magnetic field presence, and linear photon momentum transfer during radiation absorption. Gated two-dimensional tellurium devices allow one to investigate nonlinear transport for both types of carriers and in the vicinity of the Weyl point, which is not possible in bulk Te crystals, in which only the study of transport phenomena in hole systems is possible. Furthermore, our study shows that the LPGE current excited in micrometer-sized tellurene samples under similar conditions is about 30 times larger than in macroscopic bulk Te. Additionally, reduced symmetry allows for a richer set of tensor components than in higher-symmetry bulk situations. This comparison distinguishes the present observations from those previously reported for THz-driven LPGE in bulk Te [23]. The first study of nonlinear transport phenomena in tellurene explored the helicity-dependent response, resulting in a photocurrent with an opposite sign for right- and left-handed circular radiation. The present study is focused on a second order transport excited by *linearly* polarized radiation: (i) we systematically resolve the polarization-independent and linear polarization-dependent components; (ii) study their behavior upon variation of gate voltage, temperature, and radiation frequency; (iii) compare contributions along the *c* axis and perpendicularly to it; (iv) demonstrate that substantial photoresponse can be obtained at practically important room temperature; and (v) investigate intensity dependences in a wide range from W/cm^2 to tens of kW/cm^2. Unlike conventional electrode-driven nonlinear measurements, our THz excitation generates the ac electric field without applying an ac voltage through the electrodes, thereby avoiding possible artifacts associated with ac modulation of the effective gate voltage [66].

The results of the microscopic theory describe the LPGE current driven by linearly polarized radiation, see Eq. (11). Since the Stokes parameters (12) are varied in the experiments as

$$P_{\mathrm{L1}} = \cos 2\alpha, \quad P_{\mathrm{L2}} = \sin 2\alpha, \tag{21}$$

the developed theory is in agreement with the phenomenological Eqs. (3) and (4), as well as experimental results, see Figs. 2, 5, 6, and 7. In the system of C_1 point symmetry under study, all six current contributions $J^{c,a}_{0,\mathrm{L1},\mathrm{L2}}$ are nonzero and linearly independent. Indeed, a strong polarization dependence is clearly seen in Figs. 2, 5, 6, and 7. Importantly, our results reveal that the polarization-independent current components $J^{c,a}_0$ are comparable to or even larger than $J^{c,a}_{\mathrm{L1}}$, see Figs. 2, 3, 5, 6 and 7. Note that polarization-independent currents J^c_0 and J^a_0 may differ due to the in-plane anisotropy of mobility. Moreover, the terms in Eqs. (3) and (4) containing $J^{c,a}_{\mathrm{L2}} \sin(2\alpha)$, which have a maximum amplitude $J^{c,a}_{\mathrm{L2}}$ for the electric field $\boldsymbol{E}$ oriented at 45° to the *c* and *a* axes, under some conditions are comparable to $J^{c,a}_{\mathrm{L2}}$ and $J^{c,a}_0$, see dotted-dashed lines in Figs. 5, and 7 as well as the data in Figs. 6(b) and 6(c). Note that, in general, the edge currents [47,67], which behave as $J \propto \sin 2\alpha$, can contribute to J_{L2}. At the same time, in our Hall bar devices such a photocurrent is absent in the direction *a* which is perpendicular to the source-drain direction, because the source and drain contacts shunt the edges. Consequently, edge currents may contribute only to J^c_{L2} measured between the source and drain contacts. Ideally, in this geometry photocurrents excited at opposite edges would cancel each other out. However, opposite edges may have slightly different microscopic parameters, preventing complete cancellation. Therefore, strictly speaking, we cannot exclude an edge current contribution to the photoresponse. However, J^c_{L2} behaves similarly to the other five photocurrents, which supports the assumption that only "bulk" photocurrent is measured.

Microscopically, the skew-scattering, Berry curvature dipole and side-jumps contribute to all three LPGE currents $\boldsymbol{J}_{0,\mathrm{L1},\mathrm{L2}}$. In particular, the BCD contribution, Eq. (15) in components reads

$$\begin{bmatrix} j^{\mathrm{BCD}}_c \\ j^{\mathrm{BCD}}_a \end{bmatrix} = \frac{q^3\tau|\boldsymbol{E}|^2/2}{1+\omega^2\tau^2} \begin{bmatrix} D_c \sin 2\alpha + D_a(1-\cos 2\alpha) \\ -D_c(1+\cos 2\alpha) - D_a \sin 2\alpha \end{bmatrix}, \tag{22}$$

i.e., contains both the polarization-independent and two polarization-dependent contributions. The current $J^{c,a}_0$, in addition to the skew scattering, BCD and side jump mechanisms, may come from the electron gas heating by the electric field. Thermal mechanisms can be excluded as the origin of the observed photoresponse. The pyroelectric 2D camera measurements reveal a Gaussian beam with a focused spot of about 2 mm, indicating nearly homogeneous illumination across the sample. A temperature gradient generated by the contacts acting as antennas can hardly explain the observed sign reversal upon rotation of the radiation electric field. Moreover, both phenomenological and microscopic LPGE theories consistently reproduce the experimental data for different contact pairs and electric field orientations. These observations support the LPGE origin of the photoresponse. Electron-gas heating may nevertheless contribute to polarization-independent and linear-polarization-dependent currents [68].

In the representation widely used for analysis of the second order transport phenomena, the LPGE current given by Eqs. (3) and (4) is a sum of vectors perpendicular and parallel to $\boldsymbol{E}$ and—in low symmetric systems—of two additional terms

$$\begin{aligned} \boldsymbol{J} = \begin{bmatrix} J^c \\ J^a \end{bmatrix} &= \begin{bmatrix} J^c_0 + J^c_{\mathrm{L1}} \cos 2\alpha + J^c_{\mathrm{L2}} \sin 2\alpha \\ J^a_0 + J^a_{\mathrm{L1}} \cos 2\alpha + J^a_{\mathrm{L2}} \sin 2\alpha \end{bmatrix} \\ &= [\hat{z} \times \boldsymbol{E}](\boldsymbol{C}_{\mathrm{NLH}} \cdot \boldsymbol{E}) + \boldsymbol{E}(\boldsymbol{C}_{\mathrm{NLL}} \cdot \boldsymbol{E}) \\ &\quad + C^{(1)}_{\mathrm{NLD}} \boldsymbol{S} + C^{(2)}_{\mathrm{NLD}} [\boldsymbol{S} \times \hat{z}], \end{aligned} \tag{23}$$

where $\boldsymbol{S} = (2E_cE_a, E_c^2 - E_a^2)$. The term containing $[\hat{z} \times \boldsymbol{E}]$ represents the NLHE current [25–29], the contribution $\propto \boldsymbol{E}$ is the Nonlinear Longitudinal current (NLL) [23], and last two terms represent the Nonlinear Diagonal (NLD) current discussed below.

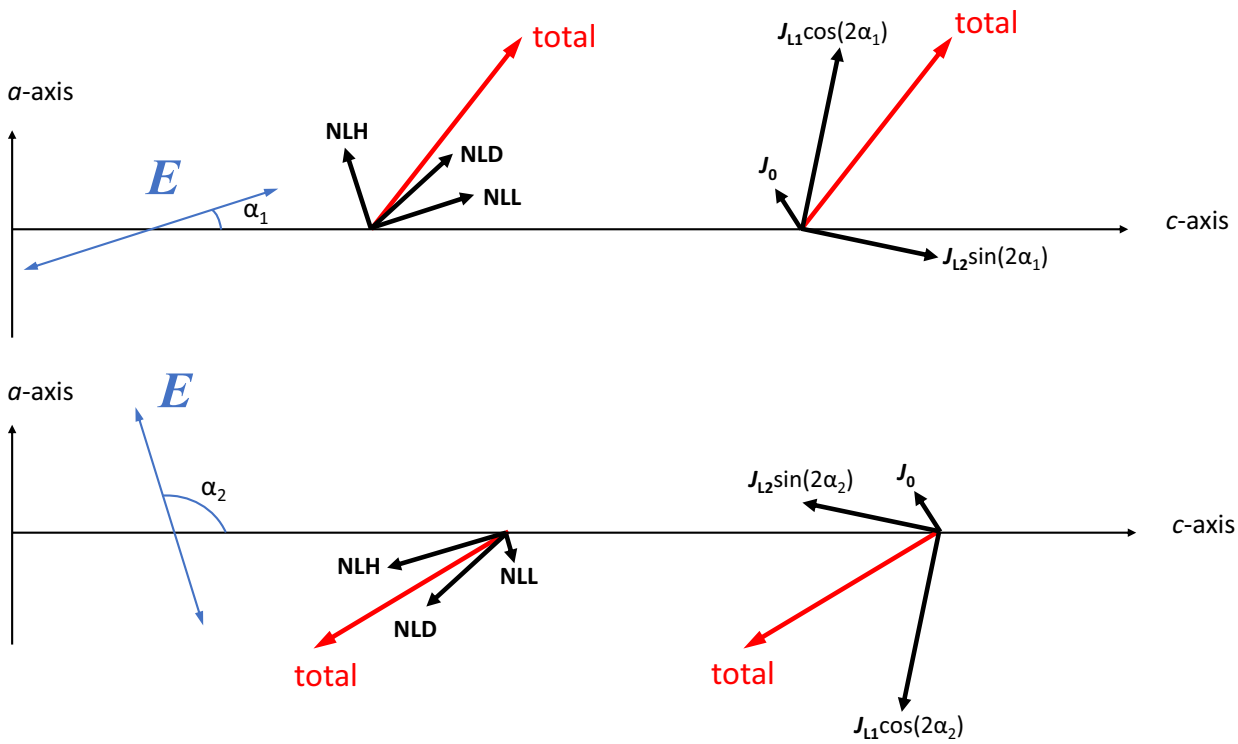


FIG. 9. Different contributions to the LPGE current for two polarization directions. Three currents correspond to the NLH, NLL, and NLD contributions in the transport representation and to the polarization-independent $\boldsymbol{J}_0$ and two polarization-dependent $\boldsymbol{J}_{\mathrm{L1,L2}}$ terms in the photogalvanic representation.

The LPGE currents $J^{c,a}_{0,\mathrm{L1,L2}}$ are related to the NLL and NLH coefficients $C^{c,a}_{\mathrm{NLL,NLH}}$ and new coefficients $C^{(1,2)}_{\mathrm{NLD}}$ by

$$C^{c,a}_{\mathrm{NLL}}|\boldsymbol{E}|^2 = J^{c,a}_0 + \frac{J^{a,c}_{\mathrm{L2}} \pm J^{c,a}_{\mathrm{L1}}}{2}, \tag{24}$$

$$C^{c,a}_{\mathrm{NLH}}|\boldsymbol{E}|^2 = \pm J^{a,c}_0 + \frac{J^{a,c}_{\mathrm{L1}} \mp J^{c,a}_{\mathrm{L2}}}{2}, \tag{25}$$

$$C^{(1,2)}_{\mathrm{NLD}}|\boldsymbol{E}|^2 = \frac{J^{a,c}_{\mathrm{L1}} \pm J^{c,a}_{\mathrm{L2}}}{2}. \tag{26}$$

The NLL, NLH, and NLD contributions to the total current for two polarization directions are shown in Fig. 9 together with a decomposition into the polarization-independent $\boldsymbol{J}_0$ and polarization-dependent $\boldsymbol{J}_{\mathrm{L1,L2}}$ LPGE currents. The behavior upon changing of the radiation polarization is described by three components, $J^{c,a}_{0,\mathrm{L1,L2}}$, which are linearly-independent in C_1 symmetry under study. Our paper establishes a connection between the photogalvanic effect well known in optics and second order nonlinear transport phenomena. Accordingly, in the transport terminology, we must introduce three independent nonlinear currents. The most widely studied transport effect is the Nonlinear Hall effect. Additionally, some studies have reported the Nonlinear longitudinal (NLL) current. To describe an arbitrary electric field completely, we must introduce a third contribution which we term the Nonlinear diagonal current (NLD). The above equations provide a linear relation between the photogalvanic and nonlinear transport contributions.

The microscopic origin of the NLHE is usually associated with the Berry curvature dipole (BCD) mechanism [25]. Indeed, the BCD contributes to $\boldsymbol{j} \perp \boldsymbol{E}$ only, see Eq. (15). At the same time, an essential contribution comes from the skew scattering [50]. The corresponding current density is discussed above and given by Eq. (11). Furthermore, the side-jump mechanism also gives rise to the NLHE [50]. The BCD and side jump mechanisms result in comparable contributions to the NLHE current whereas the skew scattering differs from them parametrically and can be dominant, see Eq. (20) and corresponding discussion. Finally, we note that the electron gas heating also contributes to NLHE as it is defined in the literature, namely $\boldsymbol{j} \propto [\hat{\boldsymbol{z}} \times \boldsymbol{E}]$, see, e.g., Refs. [25–29].

The developed theory is valid for any value of $\omega\tau$. The discussed contributions caused by different mechanisms as $\omega\tau$ increases above unity only change their magnitude because in this regime the Drude absorption decreases with increasing frequency as $\sigma(\omega) = \sigma_0/(1+\omega^2\tau_{\mathrm{tr}}^2)$. Consequently, there are no additional corrections to any microscopic mechanism. The ratio of the contributions from different microscopic mechanisms remains constant with frequency.

Furthermore, the theory, in agreement with the experiment, shows that the electric current is generated along the electric field direction $\boldsymbol{E}$, see the current values in Figs. 2, 5, 6, and 7 for angles $\alpha = 0$ (J^c) and $\alpha = 90^\circ$ (J^a). These contributions are partially caused by the Nonlinear Longitudinal current (NLL). Microscopically, this current is caused by the skew scattering and side jump mechanisms, see Sec. V. Furthermore, like the NLHE discussed above, J^c_0 contributes to the NLL current, which may have a contribution caused by the electron gas heating.

The coefficients $C^{(1,2)}_{\mathrm{NLD}}$ in Eq. (23) describe the new effect in the nonlinear transport—the Nonlinear Diagonal current. Accounting for it makes the currents $\boldsymbol{J}_{\mathrm{L1}}$ and $\boldsymbol{J}_{\mathrm{L2}}$ linearly

independent, which allows one to characterize the nonlinear transport by six linearly-independent parameters, as should be the case in systems of C_1 point symmetry. We give the name 'Nonlinear Diagonal current' ($\boldsymbol{J}_{\rm NLD}$) to the sum of two contributions in the last line of Eq. (23) because it is oriented at $\pm 45^\circ$ to $\boldsymbol{E}$ when $\boldsymbol{E}$ is parallel to c or a axes, provided $C^{(1)}_{\rm NLD} = C^{(2)}_{\rm NLD}$. The NLD current contains only polarization-dependent terms and has the value

$$J_{\rm NLD} = |\boldsymbol{E}|^2 \sqrt{\left(C^{(1)}_{\rm NLD}\right)^2 + \left(C^{(2)}_{\rm NLD}\right)^2}, \tag{27}$$

independent of the polarization direction. Microscopically, the NLD current is caused by the skew-scattering, BCD and side-jump microscopic mechanisms.

Our results show that the photocurrents excited along c and a axes have similar magnitudes, see Fig. 6. This observation is in line with theoretical expressions Eqs. (11) and (15), where the lowest possible symmetry of the system C_1 results in the same order of magnitude for all terms. Consequently, the chiral axis of the bulk Te is not special, so, for the currents excited by linearly polarized radiation, the material's chirality plays no essential role.

In our system, the skew scattering mechanism gives the LPGE current parametrically larger than the contributions due to BCD and side jumps, see the paragraph after Eq. (20). It is worth to note that the two latter have the same parameter dependencies and, in the analysis of experimental data, are indistinguishable in principle.

Our results also demonstrate that all currents $J^c_{\rm L1,L2,0}$ reverse their directions close to the CNP, when the effective gate voltage $U_{\rm G}$ changes sign, see Figs. 3 and 5(f). This agrees with the theoretical results, see Eqs. (11) and (15), where the current density is odd in the charge q. We note that, in sample B, the current's inversion point is at small positive $U_{\rm G}$. We attribute this to the presence of both types of carriers at room temperature in our narrow-gap material, which results in the simultaneous presence of the electron and hole contributions to the total current. Due to the difference of microscopic parameters for the conduction and valence bands, these currents have different magnitudes, and even for somewhat smaller hole densities, the valence-band contribution exceeds the conduction-band one.

We note that we see no specific features when the Fermi level enters the conduction band and crosses the Weyl point, where the BCD is expected to contribute significantly. The absence of a pronounced LPGE feature does not imply a vanishing BCD; rather, the BCD may be smooth or subdominant in the measured tensor component. Our estimates [see Eq. (20)] suggest that skew scattering is the dominant contribution. Since skew scattering is not expected to exhibit any anomaly when crossing the Weyl point, the absence of a feature in the LPGE data provides evidence for its dominance. In contrast, skew scattering is suppressed in circular-polarization THz nonlinear transport [23].

Our data for sample B also show that reduction of temperature results in a drastic enhancement of the current magnitude, see Fig. 5 ($T = 300$ K) and Fig. 7 ($T = 50$ and 4.2 K). The pronounced enhancement of the photocurrent upon cooling correlates with the increase in carrier mobility and transport relaxation time. Since the microscopic nonlinear response depends strongly on the scattering time, the suppression of disorder scattering at low temperatures can substantially enhance the photocurrent. In addition, in narrow-gap tellurene, electron and hole contributions coexist at room temperature and partially compensate each other, whereas at low temperatures only one carrier type remains, further increasing the photocurrent magnitude.

A difference in the spatial distribution and strength of disorder is a plausible explanation for the different relative magnitudes of the nonlinear coefficients in the samples A and B, see Figs. 2, 5 and 6, while noting that other sample-specific parameters may also contribute. Although samples A and B were grown under nominally identical conditions, their microscopic disorder landscapes and other local parameters need not be identical. A quantitative separation of disorder, strain, thickness, and electrostatic effects would require additional microscopic characterization. Furthermore, in our samples of C_1 symmetry, the direction of the total LPGE current is arbitrary and not forced to a definite crystallographic axis [69]. Thus there is no preferential direction of the photocurrent forced by the symmetry arguments, and it may exhibit a nontrivial variation with the microscopic details like disorder etc.

Finally, we address variation of the current with the radiation frequency. Figure 3 and its insets show that a decrease of ω results in an increase of the magnitudes of the current contributions $J^c_{\rm L1,0}$ normalized by the radiation power P_s. As addressed above, all currents are caused by the Drude absorption, see Eqs. (11) and (15). Therefore they are proportional to the high-frequency conductivity $\sigma(\omega) = \sigma_0/(1+\omega^2\tau_{\rm tr}^2)$. For small $\omega\tau_{\rm tr} \ll 1$, the absorbance is frequency independent, and the currents are equivalent to that obtained in dc transport measurements. While, as addressed above, in our experiments at room temperature $\omega\tau_{\rm tr}$ is somewhat smaller than unity, the insets in Figs. 3(a) and 3(b) show a clear rise of the currents $J^c_{\rm L1}/P_s$ and J^c_0/P_s with decreasing frequency. We attribute this result to the fact that the square of the THz electric field acting on carriers and causing the current in our structures, $|\boldsymbol{E}|^2$, differs from P_s by a frequency dependent factor. The reason for that is a dependence of the refractive index on frequency which is substantially enhanced in the vicinity of the reststrahlen band of tellurene. The latter is close to the frequencies used in the experiments and its position, well known for bulk Te, has not yet been studied in tellurene. Thus the frequency dependence of the currents in tellurene requires further study.

VII. SUMMARY AND OUTLOOK

We studied the direct current excited by polarized terahertz radiation in tellurene structures. This current is quadratic in the electric field and belongs to the class of nonlinear electron transport effects. We observed photocurrents that are sensitive to the orientation of the electric field vector, as well as to the gate voltage. We attribute the THz-induced currents to mechanisms arising from the low spatial symmetry of tellurene, including skew scattering, the Berry curvature dipole, and side jumps during momentum scattering. We established the equivalence between NLH, NLL, and NLD nonlinear transport currents and LPGE current contributions induced by THz radiation. The above analysis shows that measuring the

polarization dependence allows one to distinguish between various photocurrent contributions and helps one to conclude on the microscopic processes. Our results demonstrate that studying polarization-dependent THz or GHz radiation-induced photocurrents paves the way for exploring the multifaceted picture of nonlinear transport in low-dimensional and bulk semiconductor materials.

ACKNOWLEDGMENTS

The financial support of the Deutsche Forschungsgemeinschaft (DFG, German Research Foundation) via Project-IDs 564981228 (MO 5219/1-1) and 521083032 (GA 501/19) is gratefully acknowledged. Work of L.E.G. was funded by the German Research Foundation (DFG) as part of the German Excellence Strategy–EXC3112/1–533767171 (Center for Chiral Electronics). S.D.G. is grateful for the support by the European Union through the ERC-ADVANCED grant TERAPLASM No. 101053716.

Views and opinions expressed are, however, those of the author(s) only and do not necessarily reflect those of the European Union or the European Research Council Executive Agency. Neither the European Union nor the granting authority can be held responsible for them.

DATA AVAILABILITY

There are no publicly available research data or software supporting this manuscript. Requests for further information or data should be sent to the authors.

[1] W. Wu, G. Qiu, Y. Wang, R. Wang, and P. Ye, Tellurene: Its physical properties, scalable nanomanufacturing, and device applications, Chem. Soc. Rev. **47**, 7203 (2018).

[2] L. Wu, W. Huang, Y. Wang, J. Zhao, D. Ma, Y. Xiang, J. Li, J. S. Ponraj, S. C. Dhanabalan, and H. Zhang, 2D tellurium based high-performance all-optical nonlinear photonic devices, Adv. Funct. Mater. **29**, 1806346 (2019).

[3] Z. Shi, R. Cao, K. Khan, A. K. Tareen, X. Liu, W. Liang, Y. Zhang, C. Ma, Z. Guo, X. Luo, and H. Zhang, Two-dimensional tellurium: Progress, challenges, and prospects, Nano-Micro Lett. **12**, 99 (2020).

[4] G. Qiu, A. Charnas, C. Niu, Y. Wang, W. Wu, and P. D. Ye, The resurrection of tellurium as an elemental two-dimensional semiconductor, npj 2D Mater. Appl. **6**, 17 (2022).

[5] J. Zha, D. Dong, H. Huang, Y. Xia, J. Tong, H. Liu, H. P. Chan, J. C. Ho, C. Zhao, Y. Chai, and C. Tan, Electronics and optoelectronics based on tellurium, Adv. Mater. **36**, 2408969 (2024).

[6] G. Qiu, C. Niu, Y. Wang, M. Si, Z. Zhang, W. Wu, and P. D. Ye, Quantum Hall effect of Weyl fermions in n-type semiconducting tellurene, Nat. Nanotechnol. **15**, 585 (2020).

[7] G. Kim, J. Bahng, J. Jeong, W. Sakong, T. Lee, D. Lee, Y. Kim, H. Rho, and S. C. Lim, Gate modulation of dissipationless nonlinear quantum geometric current in 2D Te, Nano Lett. **24**, 10820 (2024).

[8] B. Wu, X. Liu, J. Yin, and H. Lee, Bulk β-Te to few layered β-tellurenes: Indirect to direct band-gap transitions showing semiconducting property, Mater. Res. Express **4**, 095902 (2017).

[9] C. Niu, Z. Zhang, D. Graf, S. Lee, M. Wang, W. Wu, T. Low, and P. D. Ye, High-pressure induced Weyl semimetal phase in 2D tellurium, Commun. Phys. **6**, 345 (2023).

[10] A. Apte, S. Kouser, F. Safi Samghabadi, L. Chang, L. M. Sassi, D. Litvinov, B. I. Yakobson, A. B. Puthirath, and P. M. Ajayan, Piezo-response in two-dimensional α-tellurene films, Mater. Today **44**, 40 (2021).

[11] G. Rao, H. Fang, T. Zhou, C. Zhao, N. Shang, J. Huang, Y. Liu, X. Du, P. Li, X. Jian, L. Ma, J. Wang, K. Liu, J. Wu, X. Wang, and J. Xiong, Robust piezoelectricity with spontaneous polarization in monolayer tellurene and multilayer tellurium film at room temperature for reliable memory, Adv. Mater. **34**, 2204697 (2022).

[12] S. Gao, C. Sun, and X. Zhang, Ultra-strong anisotropic photoresponsivity of bilayer tellurene: A quantum transport and time-domain first principle study, Nanophoton. **9**, 1931 (2020).

[13] Y. Wang, G. Qiu, R. Wang, S. Huang, Q. Wang, Y. Liu, Y. Du, W. A. Goddard, M. J. Kim, X. Xu, P. D. Ye, and W. Wu, Field-effect transistors made from solution-grown two-dimensional tellurene, Nat. Electron. **1**, 228 (2018).

[14] C. Niu, G. Qiu, Y. Wang, M. Si, W. Wu, and P. D. Ye, Bilayer quantum Hall states in an n-type wide tellurium quantum well, Nano Lett. **21**, 7527 (2021).

[15] P. K. Sachdeva, S. Gupta, and C. Bera, Spin Hall effect induced by strain coupling of valley and spin polarization in puckered monochalcogenide tellurene monolayer, Phys. Rev. B **107**, 155420 (2023).

[16] C. Niu, G. Qiu, Y. Wang, Z. Zhang, M. Si, W. Wu, and P. D. Ye, Gate-tunable strong spin-orbit interaction in two-dimensional tellurium probed by weak antilocalization, Phys. Rev. B **101**, 205414 (2020).

[17] C. Niu, G. Qiu, Y. Wang, P. Tan, M. Wang, J. Jian, H. Wang, W. Wu, and P. D. Ye, Tunable chirality-dependent nonlinear electrical responses in 2D tellurium, Nano Lett. **23**, 8445 (2023).

[18] B. Ma, M. Xie, L. Zhang, S. Liu, G. Ye, X. Yang, Y. Liu, F. Chu, Y. Liu, X. Zeng, X. Lu, and X. Wang, Weyl node-participated magnetoresistance and nonreciprocal transport in two-dimensional tellurene nanostructures, ACS Appl. Nano Mater. **7**, 9012 (2024).

[19] M. Suárez-Rodríguez, B. Martín-García, F. Calavalle, S. S. Tsirkin, I. Souza, F. de Juan, A. Fert, M. Gobbi, L. E. Hueso, and F. Casanova, Symmetry origin and microscopic mechanism of electrical magnetochiral anisotropy in tellurium, Phys. Rev. B **111**, 024405 (2025).

[20] P. Fontana, V. Velasco, C. Niu, P. D. Ye, P. V. Lopes, K. E. M. de Souza, M. V. Moutinho, C. Lewenkopf, and M. B. S. Neto, Quantum geometry and the electric magnetochiral anisotropy in noncentrosymmetric polar media, Phys. Rev. Lett. **135**, 106602 (2025).

[21] M. B. Silva Neto, C. Niu, M. V. O. Moutinho, P. Fontana, C. Iacovelli, V. Velasco, C. Lewenkopf, and P. D. Ye, Gate-tunable giant negative magnetoresistance in tellurene driven by quantum geometry, Nat. Commun. **17**, 5783 (2026).

[22] C. Iacovelli, P. Fontana, V. Velasco, C. Niu, P. D. Ye, M. V. O. Moutinho, C. Lewenkopf, and M. B. S. Neto, Polar

unidirectional magnetotransport in *p*-type tellurene from quantum geometry, Phys. Rev. B **114**, 165402 (2026).
[23] E. Mönch, M. D. Moldavskaya, L. E. Golub, V. V. Bel'kov, J. Wunderlich, D. Weiss, J. V. Gumenjuk-Sichevska, C. Niu, P. D. Ye, and S. D. Ganichev, Terahertz radiation driven nonlinear transport phenomena in two-dimensional tellurene, Nano Lett. **25**, 476 (2025).
[24] B. Cheng, Y. Gao, Z. Zheng, S. Chen, Z. Liu, L. Zhang, Q. Zhu, H. Li, L. Li, and C. Zeng, Giant nonlinear Hall and wireless rectification effects at room temperature in the elemental semiconductor tellurium, Nat. Commun. **15**, 5513 (2024).
[25] I. Sodemann and L. Fu, Quantum nonlinear Hall effect induced by Berry curvature dipole in time-reversal invariant materials, Phys. Rev. Lett. **115**, 216806 (2015).
[26] Y. Zhang and L. Fu, Terahertz detection based on nonlinear Hall effect without magnetic field, Proc. Natl. Acad. Sci. USA **118**, e2100736118 (2021).
[27] Z. Z. Du, H.-Z. Lu, and X. C. Xie, Nonlinear Hall effects, Nat. Rev. Phys. **3**, 744 (2021).
[28] Z. Z. Du, C. M. Wang, H.-P. Sun, H.-Z. Lu, and X. C. Xie, Quantum theory of the nonlinear Hall effect, Nat. Commun. **12**, 5038 (2021).
[29] C. Ortix, Nonlinear Hall effect with time-reversal symmetry: Theory and material realizations, Adv. Quantum Technol. **4**, 2100056 (2021).
[30] Q. Ma, S.-Y. Xu, H. Shen, D. MacNeill, V. Fatemi, T.-R. Chang, A. M. Mier Valdivia, S. Wu, Z. Du, C.-H. Hsu, S. Fang, Q. D. Gibson, K. Watanabe, T. Taniguchi, R. J. Cava, E. Kaxiras, H.-Z. Lu, H. Lin, L. Fu, N. Gedik, *et al.*, Observation of the nonlinear Hall effect under time-reversal-symmetric conditions, Nature (London) **565**, 337 (2019).
[31] Q. Shen, J. Chen, B. Rong, Y. Rong, H. Chen, X. Duan, T. Zhao, D. Guan, S. Wang, Y. Li, H. Zheng, X. Liu, X. Qiu, J. Chen, L. Cong, T. Li, R. Zhong, C. Liu, Y. Yang, L. Liu, *et al.*, Topological surface state dominated nonlinear transverse response and microwave rectification at room temperature, Adv. Funct. Mater. **35**, e06694 (2025).
[32] M. Huang, Z. Wu, J. Hu, X. Cai, E. Li, L. An, X. Feng, Z. Ye, N. Lin, K. T. Law, and N. Wang, Giant nonlinear Hall effect in twisted bilayer WSe_2, Natl. Sci. Rev. **10**, nwac232 (2023).
[33] M. Huang, Z. Wu, X. Zhang, X. Feng, Z. Zhou, S. Wang, Y. Chen, C. Cheng, K. Sun, Z. Y. Meng, and N. Wang, Intrinsic nonlinear Hall effect and gate-switchable Berry curvature sliding in twisted bilayer graphene, Phys. Rev. Lett. **131**, 066301 (2023).
[34] H. Jiang, T. Xi, J. Li, Y. He, H. Ma, Y. Mao, T. Taniguchi, K. Watanabe, D. A. Rhodes, Y. Zhang, J. Xiao, and Y. Wang, Probing interplay of topological properties and electron correlation in $TaIrTe_4$ via nonlinear Hall effect, Nat. Commun. **16**, 6351 (2025).
[35] K. Kang, T. Li, E. Sohn, J. Shan, and K. F. Mak, Nonlinear anomalous Hall effect in few-layer WTe_2, Nat. Mater. **18**, 324 (2019).
[36] S. Luo, C.-H. Hsu, G. Chang, A. Bansil, H. Lin, and G. Liang, Real space characterization of nonlinear Hall effect in confined directions, npj Comput. Mater. **10**, 40 (2024).
[37] V. I. Belinicher and B. I. Sturman, The photogalvanic effect in media lacking a center of symmetry, Usp. Fiz. Nauk **130**, 415 (1980) [Sov. Phys. Usp. **23**, 199 (1980)].
[38] S. D. Ganichev and W. Prettl, Spin photocurrents in quantum wells, J. Phys.: Condens. Matter **15**, R935 (2003).
[39] E. L. Ivchenko, *Optical Spectroscopy of Semiconductor Nanostructures* (Alpha Sci. Int. Ltd., Harrow, 2005).
[40] S. D. Ganichev and W. Prettl, *Intense Terahertz Excitation of Semiconductors* (Oxford University Press, Oxford, 2005).
[41] J. A. Zasadzinski, R. Viswanathan, L. Madsen, J. Garnaes, and D. K. Schwartz, Langmuir-Blodgett films, Science **263**, 1726 (1994).
[42] C. Niu, S. Huang, N. Ghosh, P. Tan, M. Wang, W. Wu, X. Xu, and P. D. Ye, Tunable circular photogalvanic and photovoltaic effect in 2d tellurium with different chirality, Nano Lett. **23**, 3599 (2023).
[43] E. Ziemann, S. D. Ganichev, W. Prettl, I. N. Yassievich, and V. I. Perel, Characterization of deep impurities in semiconductors by terahertz tunneling ionization, J. Appl. Phys. **87**, 3843 (2000).
[44] S. D. Ganichev, Y. V. Terent'ev, and I. D. Yaroshetskii, Photon-drag photodetectors for the far-ir and submillimeter regions, Pis'ma Zh. Tekh. Fiz. **11**, 46 (1985) [Sov. Tech. Phys. Lett. **11**, 20 (1989)].
[45] S. D. Ganichev, Tunnel ionization of deep impurities in semiconductors induced by terahertz electric fields, Physica B **273-274**, 737 (1999).
[46] S. Hubmann, S. Gebert, G. V. Budkin, V. V. Bel'kov, E. L. Ivchenko, A. P. Dmitriev, S. Baumann, M. Otteneder, J. Ziegler, D. Disterheft, D. A. Kozlov, N. N. Mikhailov, S. A. Dvoretsky, Z. D. Kvon, D. Weiss, and S. D. Ganichev, High-frequency impact ionization and nonlinearity of photocurrent induced by intense terahertz radiation in HgTe-based quantum well structures, Phys. Rev. B **99**, 085312 (2019).
[47] S. Candussio, L. E. Golub, S. Bernreuter, T. Jötten, T. Rockinger, K. Watanabe, T. Taniguchi, J. Eroms, D. Weiss, and S. D. Ganichev, Nonlinear intensity dependence of edge photocurrents in graphene induced by terahertz radiation, Phys. Rev. B **104**, 155404 (2021).
[48] P. Olbrich, L. E. Golub, T. Herrmann, S. N. Danilov, H. Plank, V. V. Bel'kov, G. Mussler, C. Weyrich, C. M. Schneider, J. Kampmeier, D. Grützmacher, L. Plucinski, M. Eschbach, and S. D. Ganichev, Room-temperature high-frequency transport of Dirac fermions in epitaxially grown Sb_2Te_3- and Bi_2Te_3-based topological insulators, Phys. Rev. Lett. **113**, 096601 (2014).
[49] M. Otteneder, S. Hubmann, X. Lu, D. A. Kozlov, L. E. Golub, K. Watanabe, T. Taniguchi, D. K. Efetov, and S. D. Ganichev, Terahertz photogalvanics in twisted bilayer graphene close to the second magic angle, Nano Lett. **20**, 7152 (2020).
[50] E. Deyo, L. E. Golub, E. L. Ivchenko, and B. Spivak, Semiclassical theory of the photogalvanic effect in non-centrosymmetric systems, arXiv:0904.1917.
[51] L. E. Golub, E. L. Ivchenko, and B. Spivak, Semiclassical theory of the circular photogalvanic effect in gyrotropic systems, Phys. Rev. B **102**, 085202 (2020).
[52] L. E. Golub and E. L. Ivchenko, Intraband circular photogalvanic effect in Weyl semimetals, Ann. Phys. **488**, 170415 (2026).
[53] E. J. König, H.-Y. Xie, D. A. Pesin, and A. Levchenko, Photogalvanic effect in Weyl semimetals, Phys. Rev. B **96**, 075123 (2017).
[54] Z. Z. Du, C. M. Wang, S. Li, H.-Z. Lu, and X. C. Xie, Disorder-induced nonlinear Hall effect with time-reversal symmetry, Nat. Commun. **10**, 3047 (2019).

[55] J. Duan, Y. Jian, Y. Gao, H. Peng, J. Zhong, Q. Feng, J. Mao, and Y. Yao, Giant second-order nonlinear Hall effect in twisted bilayer graphene, Phys. Rev. Lett. **129**, 186801 (2022).

[56] A. Bandyopadhyay, N. B. Joseph, and A. Narayan, Non-linear Hall effects: Mechanisms and materials, Mater. Today Electron. **8**, 100101 (2024).

[57] C. Xiao, Y.-X. Huang, and S. A. Yang, Lorentz skew scattering and giant nonreciprocal magneto-transport, Nat. Commun. **17**, 3632 (2026).

[58] M. M. Glazov and L. E. Golub, Valley Hall effect caused by the phonon and photon drag, Phys. Rev. B **102**, 155302 (2020).

[59] M. M. Glazov and L. E. Golub, Skew scattering and side jump drive exciton valley Hall effect in two-dimensional crystals, Phys. Rev. Lett. **125**, 157403 (2020).

[60] N. A. Sinitsyn, A. H. MacDonald, T. Jungwirth, V. K. Dugaev, and J. Sinova, Anomalous Hall effect in a two-dimensional Dirac band: The link between the Kubo-Streda formula and the semiclassical Boltzmann equation approach, Phys. Rev. B **75**, 045315 (2007).

[61] I. A. Ado, I. A. Dmitriev, P. M. Ostrovsky, and M. Titov, Anomalous Hall effect with massive Dirac fermions, Europhys. Lett. **111**, 37004 (2015).

[62] I. A. Ado, I. A. Dmitriev, P. M. Ostrovsky, and M. Titov, Sensitivity of the anomalous Hall effect to disorder correlations, Phys. Rev. B **96**, 235148 (2017).

[63] N. A. Sinitsyn, Semiclassical theories of the anomalous Hall effect, J. Phys.: Condens. Matter **20**, 023201 (2008).

[64] M. Ortenberg and R. Silbermann, Cyclotron resonance of electrons and holes in electric surface subbands of tellurium, Solid State Commun. **17**, 617 (1975).

[65] M. D. Moldavskaya, L. E. Golub, S. N. Danilov, V. V. Bel'kov, D. Weiss, and S. D. Ganichev, Photocurrents in bulk tellurium, Phys. Rev. B **108**, 235209 (2023).

[66] L. Xu, Z. Lian, Y. Wang, X. Hao, S. Yang, Y. Wang, C. Liu, Y. Feng, Y. Wang, and J. Zhang, Second harmonic generation induced by gate voltage oscillation in few layer $MnBi_2Te_4$, npj Quantum Mater. **9**, 79 (2024).

[67] S. Candussio, M. V. Durnev, S. A. Tarasenko, J. Yin, J. Keil, Y. Yang, S.-K. Son, A. Mishchenko, H. Plank, V. V. Bel'kov, S. Slizovskiy, V. Fal'ko, and S. D. Ganichev, Edge photocurrent driven by terahertz electric field in bilayer graphene, Phys. Rev. B **102**, 045406 (2020).

[68] G. V. Budkin and S. A. Tarasenko, Thermal generation of shift electric current, New J. Phys. **22**, 013005 (2020).

[69] B. Wittmann, S. N. Danilov, V. V. Bel'kov, S. A. Tarasenko, E. G. Novik, H. Buhmann, C. Brüne, L. W. Molenkamp, Z. D. Kvon, N. N. Mikhailov, S. A. Dvoretsky, N. Q. Vinh, A. F. G. van der Meer, B. Murdin, and S. D. Ganichev, Circular photogalvanic effect in HgTe/CdHgTe quantum well structures, Semicond. Sci. Technol. **25**, 095005 (2010).